



Production and detachment of oxide crystal shells on bubble walls during experimental vesiculation of andesitic magmas

P. Pleše¹ · M. D. Higgins¹ · D. R. Baker² · G. Lanzafame¹ · M. Kudrna Prašek² · L. Mancini³ · S. M. Rooyakkers²

Received: 24 October 2018 / Accepted: 14 February 2019 / Published online: 26 February 2019
© Springer-Verlag GmbH Germany, part of Springer Nature 2019

Abstract

The mutual affinity between bubbles and oxide crystals (especially magnetite) is well established and their tendency to remain in contact once they become connected (either by nucleation of one upon the other, or by attachment) has led to models of oxide transport via bubbles in natural melts. However, despite the widespread acceptance of bubble–oxide association, there is little direct textural evidence for these processes. We present results from a series of decompression experiments on andesitic melts, during which aggregates of bubbles and oxides formed because of hydrogen loss through the capsule walls causing oxidation of the melt. Experimental charges were imaged using 3D X-ray computed tomography that revealed complex bubble + oxide aggregates, with small oxide crystals coating part of the outer bubble surfaces in a shell-like morphology. These shells have smooth inner and rugose outer surfaces. Sometimes, additional concentric shells or partial shells can be found around bubbles, in the glass between the bubble wall and another shell. We quantified the volumes of bubbles and oxides and the oxides' compositions. We measured the surface area where the bubbles and oxides are in contact, thus quantifying their interface in 3D, and used these measurements to investigate the process of oxide shell formation. The complexity of the oxide textures when studied in 3D reveals a range of bubble–oxide interactions, from continuous generation, detachment and disintegration. These processes carry important implications on why such textures seem to have a low preservation potential in natural environments. Nevertheless, we have found natural samples that resemble our experimental results in a range of rock compositions from different geological environments that could have formed either due to rapid oxidation via the fluid phase or by bubbles harvesting different crystals.

Keywords Oxide transport · Bubble–crystal interactions · 3D

Communicated by Chris Ballhaus.

Electronic supplementary material The online version of this article (<https://doi.org/10.1007/s00410-019-1556-8>) contains supplementary material, which is available to authorized users.

✉ P. Pleše
pia.plese1@uqac.ca

¹ Département Des Sciences Appliquées, Université du Québec à Chicoutimi (UQAC), 555, boulevard de l'Université, Chicoutimi, Québec G7H 2B1, Canada

² Department of Earth and Planetary Sciences (EPS), McGill University, 3450 University Street, Montreal, Québec H3A 0E8, Canada

³ Elettra, Sincrotrone Trieste, S.C.p.A. S.S. 14 km 163.5 in Area Science Park, 34149 Basovizza, Trieste, Italy

Introduction

The major constituents of degassing silicate magmas are melt, crystals and gas bubbles. Each of these constituents individually provides valuable insights into magmatic evolution, such as the rate of nucleation and growth of crystals or bubbles. However, their interactions may be even more informative. Some of these interactions are well studied, such as the homogeneous nucleation of crystals and bubbles within melt (a crystal–melt and bubble–melt interaction, respectively, e.g., Fenn 1977; Kirkpatrick 1977; Gonnermann and Gardner 2013; Le Gall and Pichavant 2016; Preuss et al. 2016). Crystal–bubble interactions in magmas have received less attention, yet they may influence a variety of magmatic processes from gas storage at depth, crystal flotation and heterogeneous nucleation (Edmonds 2015; Shea 2017; Pleše et al. 2018).

Most studies on crystal–bubble interactions focused on oxides (e.g., Hurwitz and Navon 1994; Gardner and Denis 2004). Edmonds et al. (2015) investigated the 2D spatial distributions of bubbles and oxides in basalt and andesite from Soufrière Hills volcano and revealed single-point bubble–oxide contacts in the basalt, as well as multiple bubbles on larger oxide crystals, but no bubble–oxide association in the andesite. As bubbles and oxides exhibit a strong attachment force between them, they are considered to remain attached once they become connected, due to their very different chemical composition and bonding types (Mysen and Richet 2005; Gualda and Ghiorso 2007). This concept led to a recent model in which bubble–oxide pairs rise through a melt, harvesting more oxides and/or bubbles and facilitating a net transport of oxides towards the surface (Knipping et al. 2015; Edmonds 2015). Few observations of similar processes from natural rocks (e.g., Ballhaus et al. 2015) or experimental charges (e.g., Matveev and Ballhaus 2002) have been put forward. These scenarios of oxide aggregation, concentration and transport have been developed based on several key findings (Knipping et al. 2015; Edmonds 2015; Ovalle et al. 2018): (1) the existence of a single pre-eruptive bubble—multiple oxide aggregates in a natural sample, consisting of a large bubble with several smaller disconnected magnetite crystals on its surface (Gualda and Anderson 2007), (2) the affinity of single bubble–oxide pairs in experiments (Shea 2017; and references therein), and (3) the spatial distribution of sparse bubble–oxide associations in natural samples (e.g., Edmonds et al. 2015). If oxide flotation by bubbles is a viable process of oxide transport, and the attachment force between bubbles and oxides keeps them together, then why are such textures in natural degassing environments so easily overlooked?

One of the biggest obstacles in the study of bubble–crystal interactions is textural overprinting. The initial stages of texture development, and all the intermediate interactions that led to the final textures, are essentially obscured, so the exact processes behind bubble–oxide aggregate formation are not yet recognized in detail. This is especially troublesome for bubbles due to their ease of displacement in melts. Consequently, it is difficult to answer questions such as: will a bubble and a crystal attach? Will one or both change volume while attached? Under what conditions will they detach? Recent studies and advances in 4D in situ experiments have started to bridge the problem of overprinting by enabling observation of the development of a texture in real time (e.g., Bai et al. 2008; Baker et al. 2012; Voltolini et al. 2017; Pleše et al. 2018; Polacci et al. 2018), but there is still need for further research.

The aim of this study is to investigate the interactions between bubbles and oxide crystals, in andesitic melts oxidized by hydrogen loss during decompression experiments, including the dynamics of nucleation and crystallization,

bubble–oxide attachment and detachment, and aggregation. Our 3D reconstructions of experimentally decompressed melts reveal the early development of oxide–bubble aggregates, which are rarely preserved in natural systems. We compare our experimental observations with a review of natural structures from a range of geological environments and examine if they could have been produced by processes of bubble growth and magnetite crystallization.

Materials and methods

Hydrous glass synthesis

Hydrous andesitic glasses were synthesized in Au₇₅Pd₂₅ capsules in a piston-cylinder apparatus from a natural andesite crystalline rock powder (AT-29, 56.8 wt% SiO₂; Baker and Eggler 1987) after the addition of 12 wt% H₂O (the only fluid added to the starting composition). These water amounts were chosen so that the experiments are water undersaturated at the maximum pressure and temperature conditions but saturated at lower pressures (calculation based on model in Papale et al. 2006). Five to seven crushed crystal fragments were also added, of either plagioclase (An₆₇; Stewart et al. 1966), clinopyroxene (augite; Baker and Eggler 1987) or amphibole (magnesian-hornblende; Murphy et al. 2000) of approximately 0.5–1 mm³ per fragment, comprising on average 16 wt%, 30 wt% and 19 wt% of the charge, respectively. These melt and crystal compositions were chosen to represent subduction-related volcanism where andesitic melts carry phenocrysts (their exact chemical compositions can be found in Online Resource 1). The capsules were welded shut while immersed in water and stored in a 110 °C furnace for 1 h to check for water loss. Only capsules whose weight did not change were used.

Sample synthesis and decompression experiments were performed using a piston-cylinder apparatus at McGill University (Montréal, Canada). The principle behind the piston-cylinder is that force is applied on the larger piston via oil pressure. The larger piston then pushes the smaller one that in turn pressurizes the assembly. The assembly is comprised of a metal capsule in a crushable alumina-Pyrex-NaCl solid medium. Due to friction between different parts, from within the assembly to within the entire apparatus, there is a difference between the nominal and the actual pressure. To perform a friction correction and convert from nominal to actual pressure, a comparison was made between the measure nominal pressure of a selected phase transition (in the piston-cylinder) and the measured actual pressure of the same transition (in another apparatus; Baker 2004). The friction correction here is 50 MPa, and the pressure accuracy is ±25 MPa (for more details the reader is referred to Baker 2004).

Runs contained two or three capsules, each with a different added mineral phase. Capsules always contained only one mineral phase to avoid any crystal–crystal interactions. All experimental runs were isothermal at 1000 °C, and started at 650 MPa (p_1), where they were held for 1 h. The short time was used to prevent significant silicate crystal dissolution, and similar parameters were used in Baker (2004). The runs were then decompressed to a pressure p_2 (ranging from 600 to 300 MPa) for a duration of t_1 (Table 1). Decompression was performed by manually venting the piston-cylinder; there was no delay in decompressing. The decompression rates varied from 1.0 to 1.85 MPa s⁻¹. If we assume an upper crustal pressure gradient of 0.025 MPa m⁻¹ (Dziewonski and Anderson 1981), then our decompression rates correspond to 40–74 m s⁻¹, which falls within the 40–140 m s⁻¹ ascent rates of Soufrière Hills late 1997 explosive eruptions (Druitt et al. 2002). Finally, the runs were held at p_2 for a duration t_2 before isobaric quenching. The oxygen fugacity (fO_2) of melts produced using the NaCl-crushable alumina-Pyrex piston-cylinder assembly (Baker 2004) is approximately 1.5 log units above the NNO buffer, NNO + 1.5 (Dalpé and Baker 2000; Liu et al. 2007).

After quenching, the charges were removed from the capsules. The charges were not cylindrical due to non-uniform compression of the capsule during pressurization. During cooling, the charges fractured within their capsules, so upon capsule opening, they scattered. The original orientation of the fragments with respect to the vertical is unknown. The largest fragment (~ 10 mm³) retrieved from each charge was used for further analysis.

X-ray computed tomography

The largest fragment from each experimental charge (referred to as a sample hereafter) was initially imaged at the MIAM laboratory of McGill University (Montréal, Canada) using a Skyscan 1172 desktop X-ray tomography machine (Bruker, Belgium), with the aim of quickly obtaining medium-resolution 3D volumes (isotropic voxel size ~ 4 µm). The scans were reconstructed in 3D using the *NRecon* software (Skyscan 2011; <http://bruker-microct.com/next/NReconUserGuide.pdf>). Two natural samples from Krafla (Iceland) were also scanned by this machine for comparison with the experiments. The scanning conditions for all samples can be found in Online Resource 2. Samples displaying interesting textural features were selected for high-resolution imaging at the GeoSoilEnviroCARS beamline of the Advanced Photon Source synchrotron (Illinois, USA; Rivers et al. 2004, 2010). The X-ray beam was filtered to an energy of 25 keV, with an image pixel size set to 1.32 × 1.32 µm². We did not work in phase-contrast mode. The 3D reconstruction was performed with *tomoRecon* and no phase-retrieval algorithms were applied (Rivers 2012; <http://cars9.uchicago.edu/software/idl/tomography.html>).

Volume segmentation, visualization and measurements in 3D

All high-resolution scans were examined in detail for bubbles and oxides in contact with one another. Oxides were segmented in 3D by manually adjusting the threshold values

Table 1 Summary of experimental conditions during hydrous glass synthesis in a piston-cylinder apparatus

Experiment #	Charge #	Crystal type	p_1 (MPa)	p_2 (MPa)	t_1 (sec)	Decompression rate (MPa s ⁻¹)	t_2 (sec)
26	1	Clinopyroxene	650	650	0	0	0
	3	Plagioclase					
14	1	Clinopyroxene	650	600	25	1,85	300
15	1	Plagioclase	650	600	30	1,6	300
	2	Amphibole					
20	1	Clinopyroxene	650	600	50	1,0	30
	2	Amphibole					
17	1	Clinopyroxene	650	300	300	1,22	5
	2	Amphibole					
21	2	Clinopyroxene	650	300	195	1,8	0
23	2	Amphibole	650	300	210	1,62	0
24	2	Plagioclase	650	300	220	1,55	0
25	2	Plagioclase	650	300	220	1,6	0
27	1	Plagioclase	650	300	210	1,65	5

$T=1000$ °C, $p_1=650$ MPa in all experiments. Charge # is the arbitrarily assigned number to charges in multiple charge experiments, to differentiate them. p_2 refers to the lower pressure to which the experimental run was decompressed, t_1 refers to how long it took to get from p_1 to p_2 , and t_2 refers to how long the run was kept at p_2 before an isobaric quench was performed. Experiment 26 was isobarically quenched directly from p_1

(215–255 for oxides) on 8-bit volumes using the image-processing package *Fiji* (Schindelin et al. 2012). The sub-volumes of interest had to include the entire bubble and all oxides connected to it. Since each subvolume contained not only oxides in contact with a bubble, but also oxides within silicate crystals (e.g., amphibole) and solitary oxides scattered within the melt, a combination of voxel size filters in the *Pore3D* software library (Brun et al. 2010: <https://github.com/ElettraSciComp/Pore3D>), manual segmentation and 3D masking were used to segment only oxides in contact with bubbles. Quantitative analyses in *Pore3D* (Basic and Blob Analyses modules) were then performed to obtain the number and volume of these oxides.

Bubbles in contact with oxides that were located at sample centers (i.e., not at sample borders and so not potentially in contact with the capsule wall), were segmented by an automatic binarization process applied to 8-bit volumes in the *Fiji* software (threshold values of 0–105), since their volume was surrounded by either melt or oxides. Bubbles located at the sample borders were segmented using the same threshold values, however because part of their volume was in contact with the air surrounding the sample during tomographic analysis, their volume had to be manually closed to create a partial bubble volume. For each bubble, the volume of the equivalent sphere was measured by means of *Pore3D* software, from which the bubble radius was calculated. *Avizo Fire*[®] (Visualization Sciences Group) was used to merge the segmented oxide and bubble volumes in 3D and visualize them. For border bubbles with a partial volume, a sphere was created by the same software and was then scaled to fit within the real partial bubble volume. This allowed us to obtain ideal bubble volumes and measure their volume and radius, to be used in further geometrical calculations. Ideal bubble volumes were used instead of real partial volumes, because we were interested in the morphological relations between bubbles and oxides, not between bubbles and melt.

To determine the surface area of bubbles in contact with oxides, the morphology of the oxides needs to be considered. The oxides form either a spherical cap or a spherical lune (Fig. 1), where a spherical lune is a sliver of a sphere's surface, defined by two 2D sections passing through the sphere's radius (Harris and Stöcker 1998). Two different 3D measurements were done, depending on the oxide morphology. The surface area of spherical oxide caps (the most common morphology) was calculated from $S_{\text{cap w/o base}} = 2 \times \pi \times r_{\text{bubble}} \times h$ (Heath 1987), where r_{bubble} is the bubble radius and h is the height of the spherical cap. r_{bubble} was extracted by *Pore3D* or the fitted sphere volume, and h was measured as the distance between two parallel 2D sections, oriented in 3D by *Avizo Fire*[®] so that one passes through the base of the spherical cap and the other through its highest point. Where the morphology of the oxides in

contact with a bubble more closely resembled a spherical lune, two 2D sections were located in 3D so that both passed through the bubble's (or fitted sphere's) center and encompassed the oxides. The angle (α) between these 2D sections was measured in the quadrant where the oxides were located and used to calculate the spherical surface area of the lune (S_{lune}) as $S_{\text{lune}} = 2 \times (r_{\text{bubble}})^2 \times \alpha$ (Harris and Stöcker 1998).

Scanning electron microscopy

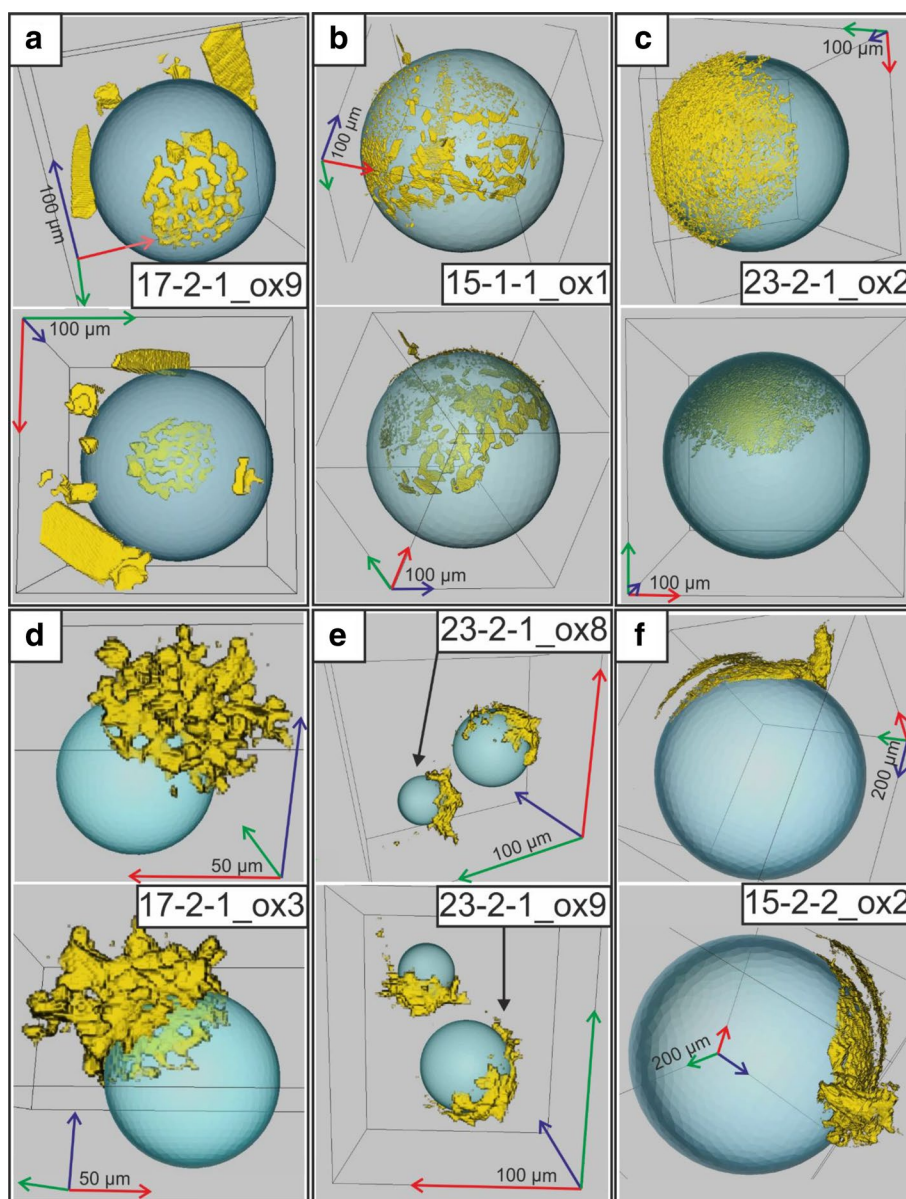
To obtain high-resolution 2D images and to ascertain the semi-quantitative chemical composition of the oxides in the experimental charges, samples from five experiments with the most interesting features were scanned at McGill University, using a Hitachi SU5000 scanning electron microscope (SEM) with an Oxford X-MAX80 energy-dispersive X-ray spectroscopy (EDS) detector and applying an accelerating voltage of 15 kV and 0.134 mA beam current. Special care was taken to grind the sample only to a target slice (known from the 3D reconstructions) where the oxide structures were located. Two natural samples from Krafla that exhibit similar oxide structures to those seen in the experiments were also analyzed for comparison. Semi-quantitative EDS analyses were performed using the *Aztec 3.3* software (Oxford Instruments).

Results

Appearance of samples and bubble–oxide aggregates within them

The samples are glassy, with silicate and oxide crystals and bubbles. The silicate crystals are rounded, and exhibit channels filled with glass, due to their partial melting at high pressure and temperature conditions (Fig. 2a). Amphibole has the largest number of such channels and they intrude furthest into the amphibole crystals (Fig. 2a). Oxide crystals vary in size and location; they occur (in order of increasing relative abundance) dispersed in the glass, as inclusions within silicate crystals (the largest 0.0012 mm^3), on bubble surfaces and along sample borders (ranging from 0.62×10^{-7} to $\sim 2.78 \times 10^{-6} \text{ mm}^3$, Fig. 2a). Bubbles also vary in size, with the largest on the sample borders ($\sim 1 \text{ mm}^3$) and smaller ones within the glass ($\sim 0.004 \text{ mm}^3$, Fig. 2a). Solitary oxide crystals dispersed in the glass did not form part of quantitative calculations. Bubble–oxide aggregates have been found in both zero-time experiments with no decompression and in experiments with different decompressions (Table 1). Here we concentrate solely on bubble–oxide aggregates, so data regarding bubble distribution, overall sample porosity, the relationship between bubbles and silicate crystals,

Fig. 1 3D visualization of seven different bubble–oxide aggregates. Bubbles are shown as transparent blue spheres, oxides are shown in yellow, and each aggregate is shown from two different orientations (two images for each aggregate). The arrow lengths of the 3D scales are the same in all three directions. **a** A bubble is in single-point contact with two tabular and two non-tabular oxide crystals, and it also has a small oxide spherical cap. **b** A bubble has a spherical cap consisting of small oxides and tabular oxides. **c** A bubble has a well-interconnected oxide spherical cap with a pronounced rugose outer surface. **d** The bubble has a spherical shell with an extremely rugose outer surface. Oxides spread equally along the bubble’s surface and outwards from it. **e** Two bubbles have oxide shells facing the same direction. Aggregates 23-2-1_ox9 (larger) and 23-2-1_ox8 (smaller) are shown together due to their proximity in the sample. **f** A bubble has two oxide layers in its shell. The layers are positioned one above the other, separated by melt, but in contact at the far-right side of the oxide cap. Both layers have a smooth inner and rugose outer side and they share the bubble’s curvature

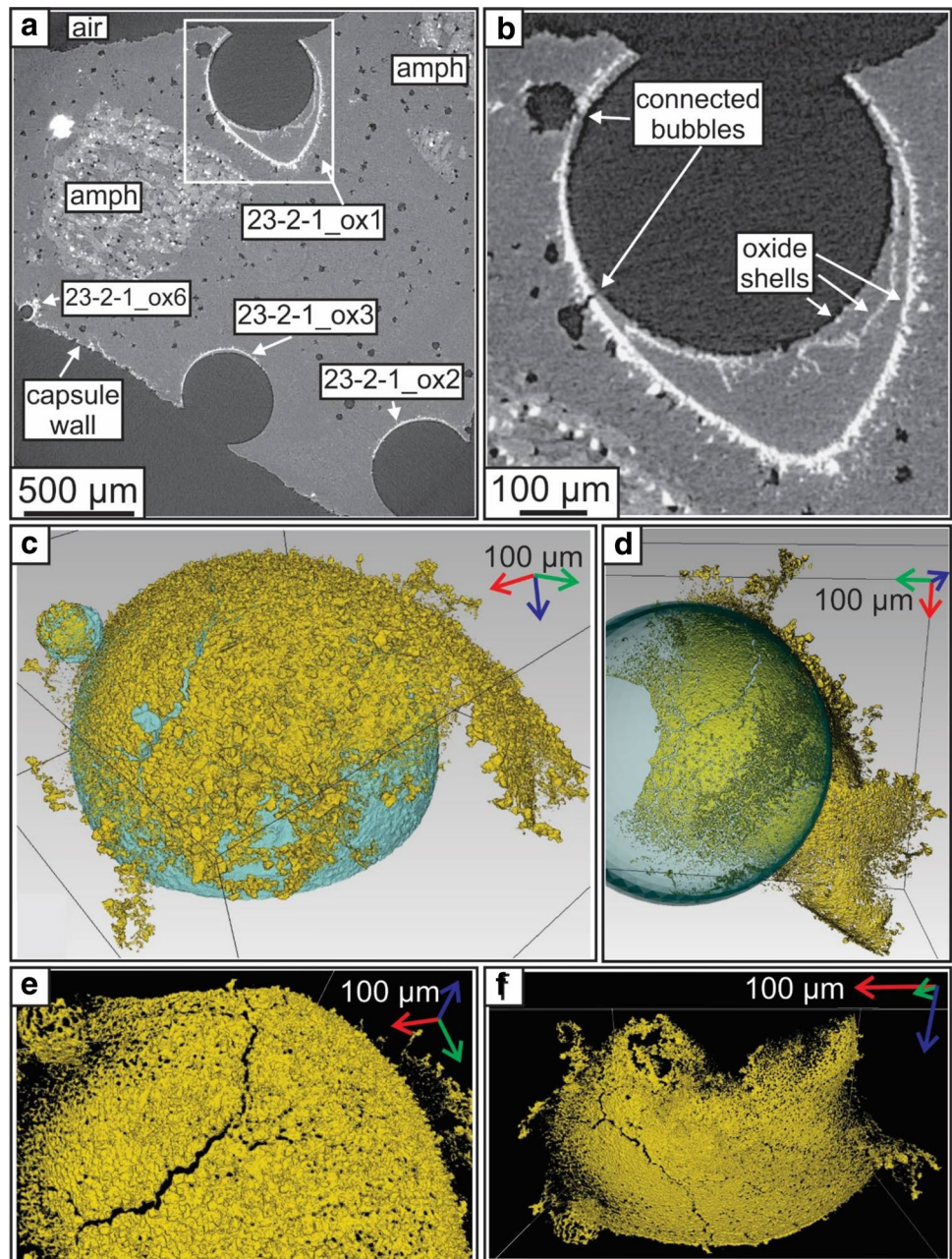


and between bubbles and melt, will be discussed in a future paper (Pleše et al. in preparation).

We define a bubble–oxide aggregate as a single bubble in contact with multiple oxide crystals (Figs. 1, 2). Bubbles in contact with a single oxide crystal were not considered, since they form a pair and not an aggregate, and accidental contact between bubbles and oxides cannot be excluded in this case. If a bubble with an oxide spherical cap or lune was also in contact with an additional single oxide crystal, then that single-point contact was only qualitatively considered. Ten experiments yielded bubble–oxide aggregates (Table 2). In total, 50 bubble–oxide aggregates were examined. Most bubble–oxide aggregates are located at the sample borders (i.e., on the capsule wall), but 20% of the aggregates were completely within

the sample (Table 2). Bubbles that line the capsule wall are here referred to as “fringe” bubbles (see Mangan and Sisson 2000; Gardner and Ketcham 2011). Aggregates were named following the convention A-B-C_oxD, where A is the experiment number, B is the capsule within that experiment, C is the identity of the sample piece retained from that capsule, and D is the bubble–oxide aggregate identified within that sample piece. The 50 aggregates identified differ in volume, location, configuration and complexity between and within capsules, but all share the same basic structure of a bubble with an outer surface covered by oxide crystals. The bubbles vary in volume, but they are always larger in volume than their associated oxide shells. Whether the shape of the shell was a cap or a lune is not related to the aggregate’s position within the sample.

Fig. 2 2D and 3D visualization of bubble–oxide aggregate 23-2-1_ox1. **a** 2D section from the 3D volume, showing four different bubble–oxide aggregates and 2 amphibole (amph) crystals. Bubbles and air are shown in black, amphiboles in light gray, silicate glass in dark gray and oxides in white. **b** Magnified section of the white rectangle from image **a**, showing only aggregate 23-2-1_ox1. The largest bubble is connected by narrow necks to two smaller bubbles. Three nested oxide shells are visible. **c, d** 3D volume renderings of 23-2-1_ox1, where the bubble is shown in blue and the oxide shell in yellow. The complex morphology of the shell includes a crack, through which the smallest bubble is connected, many apertures, a larger connected bubble, and a tear. In **d** the inner smooth surface of the shell is visible, and a large portion of the shell (lower right) is detached from the bubble surface. **e, f** 3D volume renderings of the oxide shell against a dark background. Cracks, apertures, the rugose outer surface, smooth inner surface and folding of the shell are all visible



The bubbles and their oxide shells can be in complete or partial contact. We observed three distinct configurations:

Complete bubble–oxide shell contact

In this configuration, on average 22% (ranging from 1.5 to 60%, Fig. 3b) of the bubble's outer surface is coated with oxide crystals (Fig. 1b–g). The oxide shell is not uniform in thickness and commonly has small apertures (~6 µm in diameter). The inner (bubble) side of the shell is smooth and follows the bubble's curvature. The outer (melt) side is uneven and rugose, with features such as small skeletal-like

extensions (~25 µm in length) projecting into the melt (Fig. 1d). The bubble–shell–melt contact lines are uneven in all aggregates. In some cases (e.g., 14-1-2_ox1 and 17-2-1_ox2), the bubbles had more than one oxide accumulation on their surface (oxide clusters) that were not connected to each other (Fig. 1a; Table 2).

Partial bubble–oxide shell contact

Here, aggregate shells are only partially in contact with the bubble's outer surface (Figs. 1f, 2a–d). The shells exhibit a smooth inner and rugose outer surface morphology as

Table 2 Summary of the selected geometrical parameters obtained from 3D measurements of bubble–oxide aggregates

Aggregate name	Bubbles			Oxides		
	r_{bubble} (mm)	V_{bubble} (mm ³)	Location	Oxide clusters	V_{oxide} (mm ³)	$A_{\text{oxide on bubble}}$ (mm ²)
14-1-1_ox2	0.32000	0.13725	Border	1	0.00040	0.22817
14-1-2_ox1	0.34987	0.17939	Border	25	0.00053	0.13401
15-1-1_ox1	0.18683	0.02731	Border	79	0.00031	0.19266
15-2-1_ox1	0.51288	0.56511	Border	1	0.00122	0.32155
15-2-1_ox2	0.47783	0.45699	Border	1	0.12857	0.37068
15-2-2_ox1	0.51506	0.57237	Border	1	0.00580	0.29155
15-2-2_ox2	0.51264	0.56432	Border	1	0.00574	0.42015
17-1-1_ox1	0.62941	1.04446	Border	4	0.00153	0.61039
17-2-1_ox1	0.08000	0.00214	Center	1	0.00013	0.01676
17-2-1_ox2	0.04811	0.00046	Border	13	0.00002	0.00767
17-2-1_ox3	0.03684	0.00020	Border	1	0.00008	0.00703
17-2-1_ox4	0.02246	0.00004	Center	1	0.00005	0.00258
17-2-1_ox5	0.11496	0.00636	Center	12	0.00012	0.03239
17-2-1_ox6	0.56012	0.73610	Border	1	0.00224	0.24323
17-2-1_ox7	0.04227	0.00031	Border	1	0.00007	0.00980
17-2-1_ox8	0.10431	0.00475	Center	8	0.00012	0.00000
17-2-1_ox9	0.09461	0.00354	Center	9	0.00016	0.02126
17-2-1_ox10	0.06574	0.00119	Center	1	0.00028	0.01767
17-2-2_ox1	0.68163	1.32663	Center	1	0.00238	0.23437
17-2-2_ox2	0.36834	0.20934	Border	5	0.00560	0.40958
20-1-1_ox1	0.29737	0.11015	Border	72	0.00085	0.12106
20-1-1_ox2	0.05158	0.00057	Border	1	0.00341	0.00965
20-1-2_ox1	0.09846	0.00399	Center	58	0.00031	0.02577
20-2-1_ox1	0.06032	0.00091	Border	9	0.00035	0.02690
20-2-1_ox2	0.07582	0.00182	Border	1	0.00025	0.01605
20-2-1_ox3	0.53652	0.64692	Border	73	0.00966	0.00000
21-2-1_ox1	0.29712	0.10988	Border	13	0.00072	0.14514
21-2-1_ox2	0.46128	0.41114	Border	350	0.00101	0.31782
23-2-1_ox1	0.33237	0.15380	Border	1	0.00659	0.47192
23-2-1_ox2	0.26804	0.08067	Border	1	0.00101	0.22562
23-2-1_ox3	0.19677	0.03191	Border	1	0.00116	0.18097
23-2-1_ox4	0.02124	0.00004	Border	1	0.00005	0.00339
23-2-1_ox5	0.02798	0.00009	Border	1	0.00006	0.00571
23-2-1_ox6	0.05969	0.00089	Border	3	0.00019	0.02069
23-2-1_ox7	0.03077	0.00012	Center	15	0.00001	0.00245
23-2-1_ox8	0.03085	0.00012	Border	3	0.00003	0.00379
23-2-1_ox9	0.01753	0.00002	Border	14	0.00002	0.00179
23-2-2_ox1	0.05598	0.00073	Border	1	0.00028	0.00871
23-2-2_ox2	0.21715	0.04289	Border	1	0.00643	0.25968
23-2-2_ox3	0.28562	0.09760	Border	10	0.00283	0.20057
23-2-2_ox4	0.10751	0.00520	Border	1	0.00016	0.01414
23-2-2_ox5	0.06627	0.00121	Border	1	0.00010	0.00799
23-2-2_ox7	0.06278	0.00103	Border	6	0.00007	0.00433
23-2-2_ox8	0.04384	0.00035	Border	3	0.00004	0.00066
24-2-1_ox1	0.85803	2.64609	Border	1	0.00040	0.13463
24-2-1_ox2	0.34059	0.16550	Border	1	0.00030	0.12889
25-2-1_ox1	1.15736	6.49369	Border	873	0.00280	1.05949
26-1-1_ox1	0.29034	0.10252	Border	1	0.00010	0.08451
26-3-1_ox1	0.74853	1.75680	Border	1	0.00839	0.43323
27-1-1_ox1	0.01875	0.00002	Center	1	0.00002	0.00169

r_{bubble} and V_{bubble} are the bubble radius and volume, respectively. The location of the aggregates is either the interface between the melt and the capsule or the center of the sample. For bubbles on the capsule wall, r_{bubble} is the fitted sphere radius, and V_{bubble} is derived from that radius.

Table 2 (continued)

Oxide clusters refers to the number of isolated oxide crystal accumulations on the bubble wall. V_{oxide} is the total volume of all oxide crystals on the bubble surface. A_{oxide} is the surface area of the bubble in contact with oxides

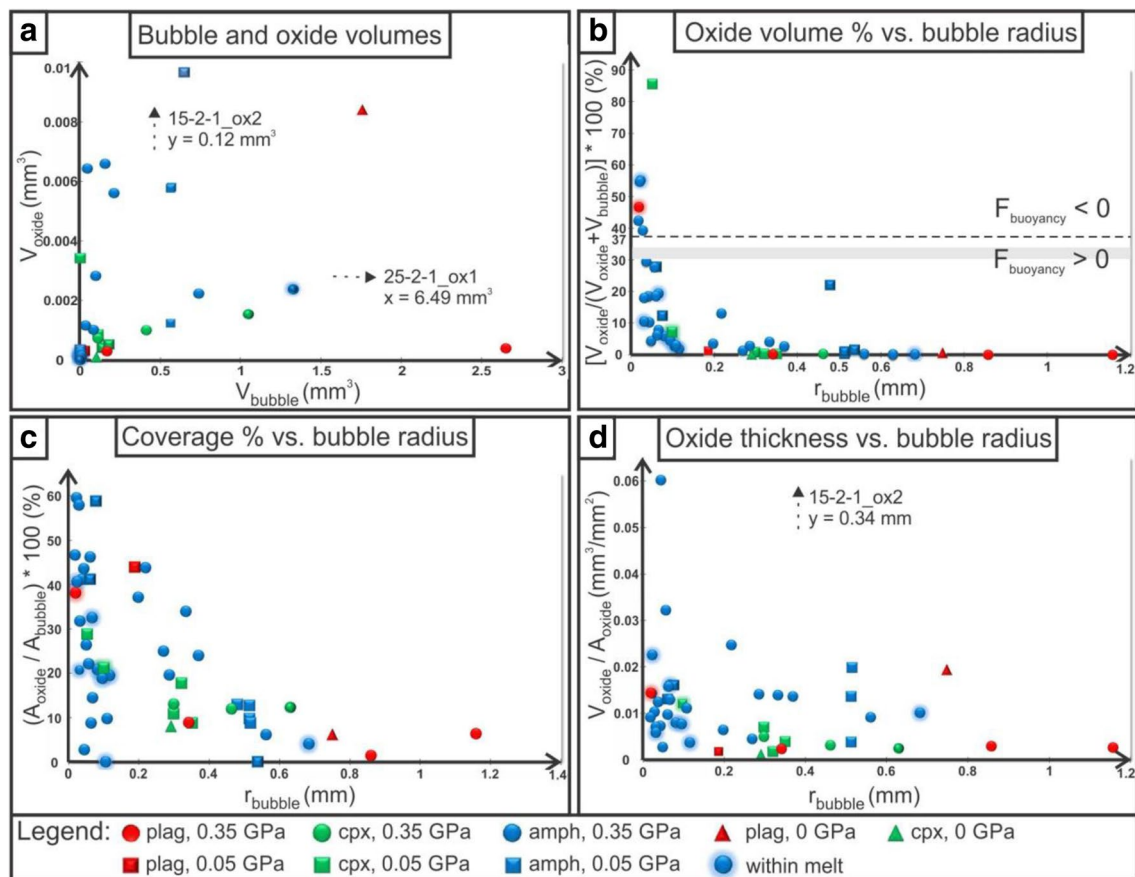


Fig. 3 Plots of geometrical data for bubble–oxide aggregates. The solid phases in the experimental change were plagioclase (plag, in red), clinopyroxene (cpx, in green) or amphibole (amph, in blue). Symbols represent different decompression drops: circles for 0.35 GPa, squares for 0.05 GPa and triangles for 0 GPa. A corona around a symbol highlights bubble–oxide aggregates found completely within the melt. The direction of an outlier location (if present) is indicated with an arrow, along with the aggregate name and the missing coordinate. **a** Total volume of all oxides in the shell vs.

bubble volume. **b** Volume percentage of oxides in an aggregate vs. bubble radius. The neutral buoyancy criteria is located at 37 vol% oxides (Knipping et al. 2015), and the gray line represents the buoyancy oxide 34–30 vol% range in our samples. **c** Oxide shell coverage of bubbles (the ratio of the surface area that the oxides occupy on the bubble and the total surface area of the bubble) vs. bubble radius. **d** Mean oxide thickness (ratio of the total oxide volume and the area the oxides occupy on the bubble surface) vs. bubble radius

in group 1, both on the parts of the shell in contact with, and away from, the bubble, as well as a range of other features including cracks, tears, folds and swirls (Figs. 1f, 2c–f). We here define a crack as an elongated aperture in the oxide shell along which the shell has split but has not separated into separate parts, and a tear as a split where the separation has begun. Regions of the shell that are furthest from the bubble are more strongly swirled and folded and have less interconnected oxide crystals. In four

cases (15-2-2_ox2 in Fig. 1f, 23-2-1_ox1 in Fig. 2a, b, 17-2-1_ox6, 23-2-1_ox6), the space between the bubble surface and the disconnected part of a shell is occupied by a second smaller and thinner oxide shell. Aggregates 15-2-2_ox2, 17-2-1_ox6 and 23-2-1_ox6 contain two such shells. In the case of 23-2-1_ox1, there are three shells in total (Fig. 2b), with the inner shells becoming progressively thinner and with less skeletal growths. The outer shell also has larger individual oxide crystals than the inner ones.

Additional single-point bubble–oxide crystal contacts

Some bubbles with oxide shells were also in contact with single oxide crystals (Fig. 1a, b). These individual oxide crystals are tabular with different orientations. These configurations were less common and so different from the aggregates that we excluded them from oxide shell volume and bubble–oxide surface coverage calculations.

In some bubble–oxide aggregates (17-2-1_ox2, 23-2-1_ox1, 23-2-1_ox6), smaller bubbles occur in contact with the rugose outer surface of the shell. These bubbles are connected to the larger bubble on the opposite (concave) side of the oxide shell via a thin neck that passes through an aperture in the oxide shell (Fig. 2b). The cross-sectional diameter of the neck is the same size as the shell aperture diameter. Some of the more spherical of these bubbles also have an oxide shell of their own (Fig. 2c).

Morphological parameters of bubble–oxide aggregates

The volumetric parameters obtained for bubbles and for oxides comprising an aggregate, and the aggregate parameters that takes both into account are presented in Table 2. Further morphological aggregate parameters are presented in Fig. 3.

The morphological data for bubble–oxide aggregates were examined in several different ways (Fig. 3). Bubble–oxide aggregates are most common in amphibole-bearing charges (70%, or 35 aggregates from 4 samples), less common in clinopyroxene-bearing charges (18%, or 9 aggregates from 5 samples) and least common in plagioclase-bearing ones (12%, 6 aggregates from 5 samples). The aggregates in plagioclase-bearing charges display the greatest variability in their morphology, while those in clinopyroxene-bearing charges are the most uniform. Since most aggregates are from amphibole-bearing charges, their distribution defines the trends in Fig. 3. One disadvantage of the comparison in Fig. 3a is that the data are clustered at small volumes. Hence, we favor the use of the bubble radius as the independent variable (Fig. 3b–d).

The volumetric ratio between the bubble and oxides within an aggregate controls the aggregate's buoyancy. The dependence of the volume percentage of oxides in an aggregate on the size of that aggregate's bubble demonstrates that the larger the bubble, the smaller the volume fraction of oxides comprising the aggregate (Fig. 3b). The horizontal dashed line at 37 vol% of oxides in a bubble–oxide aggregate represents the border between positively (<37 vol%) and negatively (>37 vol%) buoyant aggregates in andesitic melts under similar conditions, using the density values given in Knipping et al. (2015). Their calculation is based on $V_{\text{bubble}}/V_{\text{magnetite}} =$

$(\rho_{\text{magnetite}} - \rho_{\text{melt}})/(\rho_{\text{melt}} - \rho_{\text{bubble}})$, where $V_{\text{bubble}} = 1 - V_{\text{magnetite}}$, $\rho_{\text{magnetite}} = 5.2 \text{ g cm}^{-3}$, $\rho_{\text{melt}} = 2.27 \text{ g cm}^{-3}$ (Ochs and Lange 1999) and $\rho_{\text{bubble}} = 0.51 \text{ g cm}^{-3}$ for 1000 °C and 200 MPa (Pitzer and Sterner 1995; Driesner 2007; Knipping et al. 2015). In our case, $\rho_{\text{magnetite}}$ remains the same, but $\rho_{\text{melt}} = 2.07 \text{ g cm}^{-3}$ (Lange and Carmichael 1987; Ochs and Lange 1997) and $\rho_{\text{bubble}} = 0.67 \text{ g cm}^{-3}$ for 1000 °C and 650 MPa, $\rho_{\text{bubble}} = 0.45 \text{ g cm}^{-3}$ for 1000 °C and 300 MPa (using the modified Redlich-Kwong equation of state of Holloway 1987, for 650 and 300 MPa calculations). Our fluid density calculations are lower at a higher pressure, compared to Knipping et al. (2015), probably due to the low estimated concentrations of Fe and Cl in the fluid (cf., Eggler 1987 in Menzies and Hawkesworth 1986) which were omitted in our density calculations. For the pressure values of 650 and 300 MPa, we obtained 34 and 30 vol% magnetite, respectively, and the range is shown in Fig. 3b with a gray line.

This parameter can be used as a discriminant between floating and sinking of the bubble–oxide aggregate because it considers the entire aggregate, not just one phase within it. In our experiments, only six aggregates have more than 35 vol% oxides (Fig. 3b).

The dependence of oxide coverage (i.e., how much of the bubble's surface is covered in oxides) on the bubble size shows that as the bubble grows the fractional oxide coverage shrinks, i.e., small bubbles are more fully covered by oxides than larger bubbles (Fig. 3c). The oxide shell thickness on bubbles ranges between 0.002 and 0.02 mm and does not appear to be correlated with the bubble radius.

SEM analysis of experimental charges and natural samples

Semi-quantitative SEM–EDS (Fig. 4) was used to determine the chemical composition of silicate glasses and oxides. The amphibole-bearing charges have the highest average FeO_{TOT} content in the glass, 5.34 wt%, compared to 3.22 wt% in clinopyroxene-bearing and 3.96 wt% in plagioclase-bearing charges (Online Resource 1). Three different oxide groups were found within the experimental charges: oxides within silicate crystals (mainly amphibole), solitary oxides within melt (glass) and oxides that form shells on bubble walls. The glass remained andesitic and the oxides are Fe–Ti oxides; the semi-quantitative compositions are in Online Resource 1. The chemical compositions and octahedral morphologies of the oxide crystals imply oxides are magnetites. The three oxide groups are clearly distinguished by their TiO_2 contents: oxide inclusions within amphibole have the highest TiO_2 contents (9.7 to 18.5 wt%), solitary melt oxides intermediate (4.7 to 7 wt%) and the shell oxides the lowest content (2.3 to 4.2 wt%). When there are several oxide shells around a bubble, their composition is the same.

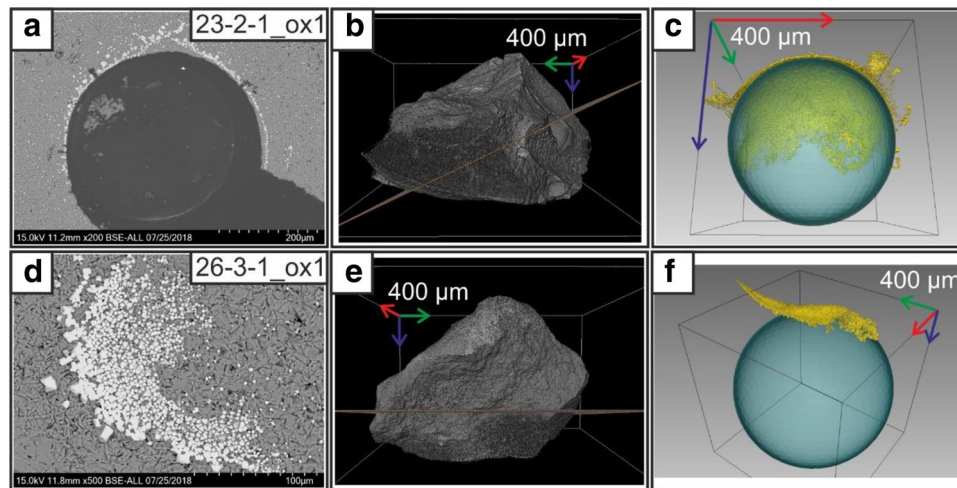


Fig. 4 Selected SEM (2D) and tomographic (3D) images for two experimental samples. **a** SEM image of aggregate 23-2-1_ox1. Oxides are present directly on the bubble surface. **b** A 3D visualization of sample 23-2-1, on which the location of the 2D plane on which the SEM analysis was performed, is indicated. The portion of the sample above this plane has been ground away for SEM analysis. **c** A 3D visualization of aggregate 23-2-1_ox1. The bubble is shown

in blue and the oxide shell in yellow. **d** A SEM image of aggregate 26-3-1_ox1. A portion of the oxide shell that detached from the (fringe) bubble is visible, along with the lack of complete oxide crystal cohesion. **e** 3D visualization of sample 26-3-1, with the location of the 2D section. **f** 3D visualization of the bubble–oxide aggregate. A large portion of the oxide shell has detached from the bubble’s surface

The glass was analyzed to investigate if there is any difference in major element compositions adjacent to the silicate crystals caused by partial melting of silicate crystals. No evidence for compositional heterogeneity of the melt was observed (compositional data is in Online Resource 1).

Discussion

Our experiments clearly show the formation of oxide crystal aggregates on the outer surfaces of bubbles in a hydrous, crystal-bearing andesitic melt. We observed bubble–oxide aggregates in experiments with and without decompression, with no difference in their morphology. We provide evidence supporting recent models invoking the role of bubbles as major oxide carriers (Knipping et al. 2015; Edmonds 2015; Ovalle et al. 2018) and offer new insights into the association and complex dynamics between bubbles and oxide crystals. Here we discuss: (1) how the oxide accumulations formed and what processes could have produced their features, (2) why these types of bubble–oxide features have not been observed before, and (3) which natural structures may have formed in a similar way.

Snapshots of dynamic processes from experimental charges frozen in time

Potential harvesting of oxides originating from the melt or the amphiboles

Harvesting of oxides by bubbles is considered by many authors to be the main method of oxide accumulation on bubbles and subsequent transport in natural melts (Knipping et al. 2015; Edmonds 2015; Ovalle et al. 2018), so it is worth examining whether harvesting could have occurred in the experiments. By harvesting, we mean the process of attachment of a pre-existing oxide to a pre-existing outer bubble wall. For oxide harvesting to occur, oxides must be present in the melt and the bubble walls must move with respect to the melt via bubble growth or buoyant rise.

Bubbles with oxide shells in our samples display a range in size (Fig. 3), thus implying that bubbles were growing during decompression. Since there are solitary oxide crystals within the melt, the bubbles could have harvested them during growth. Sample edges, where the melt was in contact with the capsule, are lined with solitary

disconnected oxide crystals and are also the location of the largest bubbles, which likely nucleated heterogeneously on imperfections of the AuPd-capsule wall (Fig. 2a). The larger size of the fringe bubbles likely reflects degassing of melt in the interior of the capsule by water diffusion into the fringe bubbles prior to decompression (Mangan and Sisson 2000). There is no evidence of fringe bubble movement through buoyancy or melt convection. If fringe bubbles moved along the capsule wall, we would expect more oxides on their advancing side (and that would indicate the “up” direction). Since we do not observe this, we assume they stayed in place.

Most bubble–oxide aggregates, as well as the largest and most elaborate oxide shells, were found in samples containing amphibole (Fig. 3) and these samples also contain the highest average FeO_{TOT} wt%. Amphibole crystals exhibit more melting than the other crystals in our experiments and contain more oxide inclusions (already present in the amphiboles prior to our experiments; Fig. 2a) than the plagioclase and clinopyroxene crystals (in their respective charges). The partial melting of amphiboles (at maximum P and T) increased the FeO and MgO content of the melt (to 5.5 and 2.2 wt%, respectively) compared to the melt in plagioclase- and clinopyroxene-bearing charges (to 3.96 wt% FeO and 0.8 wt% MgO in plagioclase-bearing, 3.22 wt.% FeO and 0.9 wt.% MgO in clinopyroxene-bearing charges, Online Resource 1), where crystals melted much less. Consequently, most aggregates are found in amphibole-bearing charges.

During partial melting of the amphiboles, their oxide inclusions could have become incorporated into the melt. Since our 3D imaging took place after the experiments were completed, we cannot rule out that this process was a source of the oxides that were then harvested by growing bubbles. However, first, if this was the case, we would expect the melt around the amphiboles to contain some solitary oxides and a greater abundance of bubble–oxide aggregates around the amphibole; we see neither of these features. Second, the oxides that remained within the amphibole display a range in size, and some are much larger than the oxides comprising the shells (Fig. 2a). Third, if amphibole was the main source of oxides, we would not expect to see bubble–oxide aggregates in samples containing plagioclase or clinopyroxene. Fourth, there is a difference in Ti content in the oxides within the amphibole, within the melt and on the bubble surface. Fifth, harvesting would not produce such a smooth inner and rugose outer shell surface, but instead both surfaces would be at least somewhat rugose, due to the random orientation of the harvested oxides towards the bubble surface. We thus conclude that harvesting of oxides originating from the amphiboles or crystallized from the melt was not the main process responsible for the generation of oxide shells.

In situ crystallization of oxides on bubble walls

If crystal harvesting was not significant, then oxides must have crystallized at the bubble–melt interface. Hence, we must examine the argument for in situ oxide crystallization as the dominant mechanism for production of the oxide shells.

Gualda and Anderson (2007) have suggested that crystallization of magnetite on bubble walls could occur in natural melts. At 1000 °C, hydrogen diffuses through the AuPd-capsule wall much faster than oxygen (Jakobsson 2012). This loss of hydrogen forces the reaction $\text{H}_2\text{O} \rightleftharpoons \text{H}_2 + \frac{1}{2}\text{O}_2$ to the right-hand side to preserve equilibrium, thus prompting the dissociation of water molecules within the melt and an increase of oxygen fugacity. Consequently, the melt near the capsule wall becomes locally oxidized, which prompts the precipitation of magnetite. The presence of FeTi oxides in our andesitic samples most likely caused a local decrease in f_{O_2} (Lange and Carmichael 1996), but since their crystallization occurred below 1070 °C, f_{O_2} should still be very close to NNO + 1.5 (Dalpé and Baker 2000; Liu et al. 2007).

The bubble wall represents the interface between the bubble and the melt. As the bubble grows, and H_2O from the melt diffuses through the bubble–melt interface, the melt around it becomes oxidized and supersaturated in magnetite components. This prompts the crystallization of magnetite, more likely on the bubble wall than near it, since heterogeneous nucleation (on a surface) is energetically favored over homogeneous nucleation within the melt (Hurwitz and Navon 1994). The nucleation of different silicate mineral phases on bubble walls has already been reported (e.g., plagioclase, Applegarth et al. 2013; amphibole and plagioclase; Rooyackers et al. 2018), so the process should be applicable to an oxide phase such as magnetite, in both experimental and natural environments.

A further argument for in situ crystallization is the morphology of the oxide shells; their smooth side faces the bubble and the rugose side containing skeletal growths faces the melt. The position of the skeletal growths and the detached shell parts points unequivocally to the shell occupying the outer side of the bubble and originating from the melt. If it were otherwise (on the inner bubble side), the skeletal growths would be facing inward, towards the center of the bubble. The shell itself could then also not detach since that would require the oxides to cross from within the bubble into the melt, breaking the bubble’s surface and surmounting its surface tension. This scenario is energetically unfavorable and therefore unlikely.

Figure 3b, c show that bubbles with a radius from 0.05 to 0.4 mm have either more voluminous shells, or larger fractional shell coverage compared to larger bubbles. The former could indicate that after an initial spreading of oxides on the bubble surface, oxide outward growth towards the melt

becomes more favorable. If the spreading mechanism was harvesting, we would expect a linear dependence between the bubble volume and oxide volume in Fig. 3a, or between the bubble radius and oxide thickness in Fig. 3d, and that is not the case. Thus, this points to oxide in situ crystallization. The fact that the oxide volume percentage decreases as the bubble becomes larger (Fig. 3b) could be because oxides form a two-dimensional shell around a three-dimensional bubble. This could also explain the lack of correlation between the oxide thickness and bubble radius (Fig. 3d). As the mean thickness of the oxide rims remains approximately constant (Fig. 3d), the outward growth must mainly occur as narrow skeletal crystals or by the generation of new shells. Both increase the oxide volume without increasing the oxide coverage.

Bubble breakup via daughter bubble generation through an oxide shell aperture

The connected bubbles seen in aggregates 23-2-1_ox1 (Fig. 2b, c) and 17-2-1_ox2, have not yet been reported in geological environments to our knowledge. We cannot envision a scenario where two bubbles would coalesce by forming a neck through the oxide shell, since creating such a shape would necessitate energy consumption, so we infer that this instead reflects bubble breakup. We see no similarity to spanning clusters (Candela 1991). The larger bubble facing the smooth concave inner oxide shell side is the primary, or “parent”, bubble, and the smaller bubble on the rugose, convex, outer side of the shell is the newly generated secondary, or “daughter” bubble. Here we chose the term daughter bubble to emphasize the connection between the two bubbles, and so we will refer to this bubble breakup scenario as daughter bubble generation. Bubbles found in contact with the rugose shell side, but with no bubble neck connection to the bubble on the inner side, are not considered daughter bubbles. They are also not former daughter bubbles, since a small bubble volume is expected to remain in the shell aperture after daughter bubble detachment (as seen in Gnyloskurenko et al. 2003). We suggest that daughter bubbles form as a response to decompression-induced bubble expansion coupled with the rigidity of the oxide shell (the rigidity is demonstrated by the cracks). With decreasing pressure, a bubble partially covered with an oxide shell will attempt to expand against its rigid shell. Apertures in the rigid shell may then be exploited as gateways for bubble expansion; the apertures become leakage points. We can envision multiple apertures acting as gateways, but since bubble breakup is energetically unfavorable as more surface is generated, as opposed to less, one aperture could prevail over others. This is supported by our experiments; where multiple daughter bubbles are present, they have a

large volume differences between them (Fig. 2b), indicating that for a discrete pressure drop, a single aperture is “activated”. We suggest expansion occurs through apertures rather than on the part of the bubble not covered by oxides because circumventing the shell would produce a non-spherical shape, and, in our experiments, because it is prevented by the capsule wall.

The appearance and location of daughter bubbles are evidence that oxide shells are not a quench texture and point to a timeline of events: parent bubble formation, oxide shell formation, daughter bubble formation through apertures, and formation of oxide shells on daughter bubbles (Fig. 5). If the (parent) oxide shells were a quench texture, we would not see daughter bubbles or their shells. All daughter bubbles have a narrow cylindrical neck, including the one daughter bubble connected through a shell crack. Thus, the crack in the oxide shell must have formed after the daughter bubble, otherwise the neck would not be cylindrical. Since the cracking of the oxide shell was induced by parent bubble expansion, it is also not a quench texture.

Daughter bubble generation is a process opposite to bubble coalescence, so it increases the number of bubbles present. Daughter bubble formation is controlled by the decompression rate, the aperture diameter and the volume of the space beneath the aperture (based on Gnyloskurenko et al. 2003, in an aqueous system). The latter is here equivalent to the parent bubble volume. The daughter bubble’s volume and shape also depend on the magnitude of decompression, as well as on the wetting conditions and surface properties of the oxides (Gnyloskurenko et al. 2003). In a silicate melt, oxides and bubbles readily wet each other’s surfaces (Hurwitz and Navon 1994). In our experiments, the oxide shell’s outer surface is very rugose and the parent bubble’s volume is much larger than the aperture diameter. It seems that at our decompression rates, surface phenomena dominate so the wetting conditions at the aperture control the daughter bubble’s final volume and shape. Thus, in the case of oxide shell apertures where wetting is favorable, the daughter bubble grows spherically. The daughter bubbles in our samples are mostly spherical and we can clearly see a neck, (Fig. 2b), so detachment by neck rupture is expected to follow (Gnyloskurenko et al. 2003). The detachment of a daughter depends on the balance between the buoyancy forces acting upward and the surface tension forces acting downward on the daughter bubble (Gnyloskurenko et al. 2003). The subsequent processes of neck rupture and detachment were not observed in our experimental run products. After detachment, some bubble volume is likely to remain in the aperture (i.e., part of the neck, as seen in Gnyloskurenko et al. 2003), leading to possible continuous generation of multiple daughter bubbles through the same aperture.

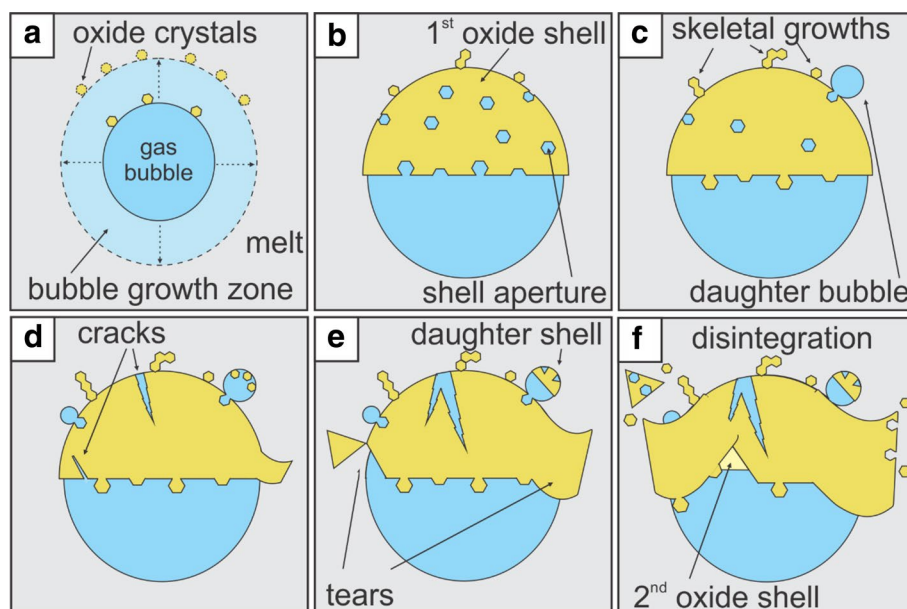


Fig. 5 Summary of observations of bubble growth and oxide shell development. **a** On the surface of a bubble growing within the melt, oxides start to crystallize due to hydrogen diffusion and resultant melt oxidation. **b** As the processes continues, oxides become more and more interconnected and create an oxide shell on the bubble wall. **c** A complex oxide shell is formed with apertures, an uneven border and skeletal outward growths. Daughter bubbles form by fluid leaking

through the apertures. **d** Cracks form in the oxide shell, and daughter bubbles may start to develop oxide shells of their own. **e** The cracks widen, and some become the starting point of oxide shell tearing. **f** After some time, the first oxide shell starts to detach from the bubble and disintegrates, whilst the newly available bubble surface becomes the location for the generation of a new oxide shell

Stability of bubble–oxide aggregates through attachment and detachment

The ascent of bubbles through a melt is most relevant for the degassing of magmatic systems and the rising or sinking of crystals for the formation of ore deposits (e.g., magnetite, Knipping et al. 2015; Ovalle et al. 2018; or chromite; Matveev and Ballhaus 2002; Ballhaus et al. 2015). However, if we consider the buoyancy of pairs of different phases (or multi-phased aggregates), here bubbles and crystals, their stability will influence their dynamics. We discuss this stability through interactions, i.e., attachment and detachment forces acting on the aggregate in question (Gualda and Anderson 2007). Interactions between a bubble and any particle can be divided into three types: collision, attachment and detachment (Phan et al. 2003). In evaluating the stability of our bubble–oxide aggregates, we will only consider attachment and detachment, as collision applies only to harvesting, which we argued above is not occurring in our experiments.

Bubbles and oxides that form pairs or aggregates wet each other's surfaces very well and are held together by surface tension forces. Since the surface energy release is highest when they are joined, once they become attached, a large amount of energy (larger than for silicates and bubbles) will need to be spent to detach them (Gualda and Ghiorso 2007).

Gualda and Ghiorso (2007) define the attachment energy between bubbles and oxides as the summation of the adhesion and deformation energy (when a bubble deforms from a sphere to a spherical cap when attaching to a crystal surface). Our oxide shells are much smaller in volume than the bubbles they wet, so bubble deformation is insignificant, and the adhesion energy dominates.

We have found examples of phenomena such as we see in our experiments in the studies of surfaces and mineral processing (e.g., Gnyloskurenko et al. 2003; Phan et al. 2003). We have identified examples similar to our observations and here we apply them to a silicate melt environment. The region of the bubble where bubble and oxides are most strongly attached is the maximum adhesion area (Fig. 6b–d) and is defined by the angle θ_1 ($< 90^\circ$, from the vertical, see Phan et al. 2003) shown in Fig. 6b. There the adhesive force between the bubble and the oxides is at a maximum (Phan et al. 2003). Consequently, even though oxides could crystallize anywhere on the bubble wall, they will remain in place only within this area, and oxide shells are most likely to form from these oxides. The configuration of our oxide shells, in a spherical cap morphology, supports this (Figs. 1, 2) and the value of θ_1 in our aggregates varies from 13° to 86° , with a mean and median of 55° calculated from $\cos\theta_1 = (r_{\text{bubble}} - h)/r_{\text{bubble}}$ and confirmed by 3D measurements (h is the height of the spherical cap).

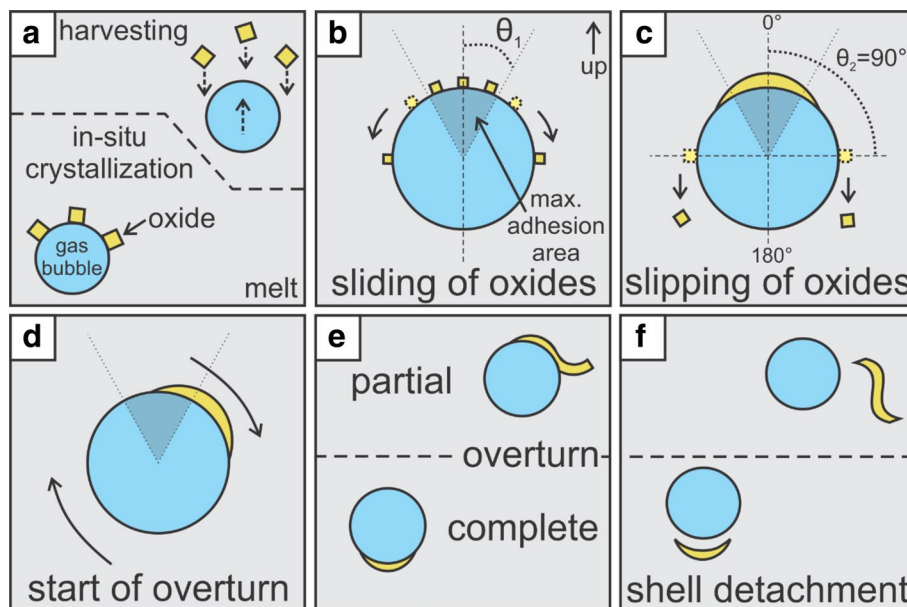


Fig. 6 Schematic representation of the behavior of bubble–oxide aggregates in relation to the maximum adhesion area. All images are vertical sections with up at the top. **a** Bubble–oxide aggregates form, either via in situ crystallization on the bubble wall or via harvesting. **b** Oxides within the maximum adhesion area are stable, whereas those outside it start to slide downwards on the bubble wall. **c** An oxide shell forms within the maximum adhesion area. Due to crystal

adhesion, parts of the shell can exceed the adhesion area and become detached. **d** Due to the oxide shell’s weight, the entire aggregate becomes mechanically unstable and overturns. **e** If overturn is faster than detachment, the oxide shell will finish on the opposite side of the bubble. If the overturn is only partial, detachment will start before complete overturn occurs. **f** The extent of the overturn governs the style of detachment

Contrary to attachment, which can be examined when two phases are in contact, detachment is much more difficult to examine in post-process samples, even in 3D. It is difficult to state that two distinct phases have detached if they are not directly observed to transition from an attached to a detached state. We observed several features in 3D that we interpret as the start of oxide shell detachment (Fig. 2): (1) parts of shells not in contact with a bubble surface have smooth inner and rugose outer surfaces and the same concavity as the bubble, (2) several shells may be present on the same bubble, separated by melt, and (3) cracks and tears occur in most oxide shells. We see such detachment features on aggregates that are positively buoyant: 23-2-1_ox1, 23-2-1_ox6, 15-2-2_ox2 and 17-2-1_ox6.

Phan et al. (2003) proposed that the capillary force, the particle’s weight and turbulent inertial forces caused by the aggregate’s movement govern detachment. We assume the turbulent contribution within the experimental charges as minimal, as we did not observe evidence of fringe bubble displacement. Additionally, detachment is easier for particles outside the maximum adhesion area (Fig. 6b, c), which in our aggregates most commonly is $\theta_1 = 55^\circ$. The ease of detachment seems particularly important for our case, since due to crystal adhesion, oxide shells would behave like sheets rather than like individual particles. If one part of the shell extended beyond the maximum adhesion area boundary

(Fig. 6c), e.g., when sideways oxide growth is faster than bubble growth, detachment could begin, and when part of the shell is detached, the rest starts to peel off (Fig. 6e, f). If detachment starts by oxides sliding on the bubble surface, when they reach $\theta_2 = 90^\circ$, they will detach from the bubble wall, rather than continuing on the bubble surface until they reach 180° because the equator is the weakest region, not the bottom of the bubble. Another possibility is that the oxide shell becomes so thick or envelops so much of the bubble’s surface (i.e., outward or sideways oxide growth surpasses bubble growth), that the aggregate overturns (Fig. 6d), leaving the uncovered (shell-free) part of the bubble is facing upwards and free to detach by its own buoyancy (Fig. 6e, f).

Bubble–oxide aggregates with multiple oxide shells

One of the most intriguing structures we observed are multiple oxide shells around a single bubble (Fig. 2). We envision two possible origins for these. The first possibility is that all shells originate from a single shell that has delaminated, and the second is that all shells originated from the same bubble wall but formed incrementally over time (i.e., the shell furthest away from the bubble is the oldest and the one closest to it is the youngest). We favor the second mechanism because all oxide shells share the same concavity as the adjacent bubble, and have smooth inner sides and rugose,

outer sides that could only form if the oxides crystallized against a smooth surface (i.e., a bubble wall). For the latter reason, we also reject the comparison to Liesegang bands, since they exhibit only rugose surfaces (Boudreau 1995, see his Fig. 8). We therefore regard multiple nested shells around a single bubble as reflecting multiple generations of shells. The different sizes of oxide crystals in separate shells most likely reflect their growth time. The presence of multiple shell generations around a single bubble provides further evidence for detachment. This may occur either as the first (oldest) shell becomes too large and outgrows the maximum adhesion area, or as the bubble's volume or shape oscillates and displaces the rigid shell. In nature, slight pressure changes are constantly occurring in magmatic systems, driven by both internal (such as localized convection) and external (such as pressure waves passing through the melt) forces, causing bubble volume oscillations or vibrations (e.g., seismic waves; Ichihara et al. 2004). Such slight pressure oscillations are also present in our experiments due to the manually controlled decompression (through slight valve opening). Once detachment from the bubble starts and melt begins to percolate in the newly available space between the detached shell and the bubble, a new shell can form.

Preservation potential of oxide shells

The presence of many apertures in our oxide shells indicate that once detached the shells easily disintegrate, as suggested by Edmonds et al. (2015). Away from the bubble wall, the shells can be easily disrupted (e.g., by colliding with other crystals or bubbles, or by movement of the host melt). The disintegration is already visible in Fig. 2c–f, in the part of the shell away from the bubble, presumably caused by the lack of a stabilization by the bubble wall. It seems that the unique morphology of the oxide shells enhances their disintegration. Some cohesion must be present between individual oxide crystals within the shell, otherwise they would immediately detach individually from the bubble, but it is present only in two directions since the shells have a sheeted morphology. Forces (e.g., shear, Kushnir et al. 2017) from any direction apart from within the plane of a detached shell could thus be sufficient to cause disintegration. This implies a low preservation potential for detached shells. We infer that this poor preservation potential, coupled with a lack of 3D observations, could be the reason why intact oxide shells have not previously been described in natural or experimental samples.

Despite their low potential for preservation, detached oxide shells need not disintegrate completely into individual crystals. Several crystals that have remained aggregated even after shell disintegration can be seen in Fig. 2c–f. Such crystal aggregates could coarsen into larger crystals or

crystal clusters and become the precursor for larger oxide accumulations.

Occurrences of analogous structures in geological materials

We have shown that oxide (magnetite) shells can form in experimental charges by crystallization from the silicate liquid at the bubble–melt interface, due to oxidation of the sample by hydrogen loss. Oxidation via hydrogen loss does occur in magmatic systems (e.g., Vollinger 2017), and hydrogen loss via diffusion is present in natural systems with a remote link to the surface (e.g., Myers et al. 2019), which leads to the question of whether oxide shells can form around more oxidized fluid or vapor bubbles in natural magmatic systems?

We hypothesize that the low preservation potential of the oxide shells commonly masks evidence for their formation in nature, either by in situ crystallization or by harvesting. Here we review evidence for analogous structures from a range of geological environments that we believe are by nucleation and/or aggregation of crystals on a spherical interface (bubble–melt or melt–melt). Two textural observations are unique to all examples: the possible occurrence of multiple nested shells within the silicate liquid, and the combination of a smooth inner and rugose outer surface of the shells. We also present our own example of natural textures in granophyres from Krafla volcano (Iceland) that we infer were formed by a process of shell formation on bubble surfaces, similar to our experiments. We will start with natural examples that most resemble our experimental charges and proceed to examples that may be formed by either in situ crystallization or harvesting.

Krafla granophyres

Natural textures within granophyres from Krafla display some remarkably similar features to our experimental oxide shells. Textures in two granophyre xenoliths, KR-7 and KR-19, from Krafla volcano (Iceland) were examined. The samples are derived from shallow felsic intrusions and were ejected in 1724 during the formation of Víti, a small maar crater in the central region of Krafla caldera (Sæmundsson 1991; Jónasson 1994). Whole-rock compositional data for these samples is not currently available, but similar samples from the Víti crater analyzed by Jónasson (1994; his Table 1) have SiO₂ contents ≥ 73.70 wt%. The samples have a mineral assemblage of plagioclase + clinopyroxene + magnetite hosted in a granophyric groundmass (intergrown alkali feldspar + quartz).

In 2D sections (SEM and tomographic), the structures of interest appear as linear or curved crystal aggregates (Fig. 7a–c). EDS analysis was performed on polished thin

Fig. 7 SEM and tomographic images for natural sample KR7 from Krafla. **a** SEM image of a clinopyroxene (cpx; light gray) and magnetite (mgt; white) aggregate within a granophyric groundmass (mottled light and dark gray). The elliptical structure is ~800 μm across. **b** SEM image of another accumulation of the same assemblage, with a more pronounced sphericity. It has a smooth inner and rugose outer surface. The relationship between the cpx and mgt crystals is more clearly visible, with skeletal cpx and mgt crystals projecting outward from the convex side. **c** 2D section from the 3D tomographic volume of sample KR7. Oxides are the brightest feature in the image, cpx is light gray and the granophyric groundmass is dark gray. Both linear and curved structures are visible, two of which are zoomed in on (insets; c1 and c2). **d** A 3D visualization of several curved mgt–cpx structures, manually segmented from the sample volume. Mgt and cpx are not visualized individually to simplify the visualization

sections of the Krafla samples to identify the mineral phases forming the curved structures. The oxides are magnetite, and the silicate phase is clinopyroxene. In reconstructed 3D volumes (Fig. 7c, d), we observe shell-like spherical structures with a smooth inner (concave) surface and rugose outer (convex) surface with skeletal projections similar to our experimental oxide shells.

These structures are not observed in association with bubbles, but a process similar to that forming the experimental oxide shells could create spherical structures with such surfaces, due to the proximity to the atmosphere, which could result in rapid oxidation. Rapid growth of crystalline phases without the presence of a bubble would not lead to structures with a smooth inner surface, since they would have nothing to grow against. The smooth inner and rugose outer surfaces of these structures favor in situ crystallization of magnetite and clinopyroxene on the outer bubble walls over harvesting. The absence of bubbles in post-process samples could be explained by bubble loss via detachment and buoyant rise, and the subsequent infilling of the space left behind by the melt. We suggest that these “ghost bubble” structures were preserved due to the presence of clinopyroxene, which is found between magnetites, and potentially prevented the shell disintegration. The clinopyroxene microlites seem to have also crystallized on the bubble wall, since they exhibit a smooth inner and a jagged outer surface. We see, however, some structural relaxation, since some structures are planar and no longer spherical. Since the degree of structural relaxation is unknown, the present circumference and shell sizes do not indicate the original bubble size.

Micrometeorites

Shell-like Fe–Ni oxide accumulations (of unspecified mineralogy) have been described on the outer surfaces of gas bubbles in partially molten micrometeorite interiors (Toppani et al. 2001; Taylor et al. 2011). Micrometeorites are interplanetary dust particles recovered from Antarctic ice or deep-sea sediments. The Fe–Ni oxide shells exhibit a smooth

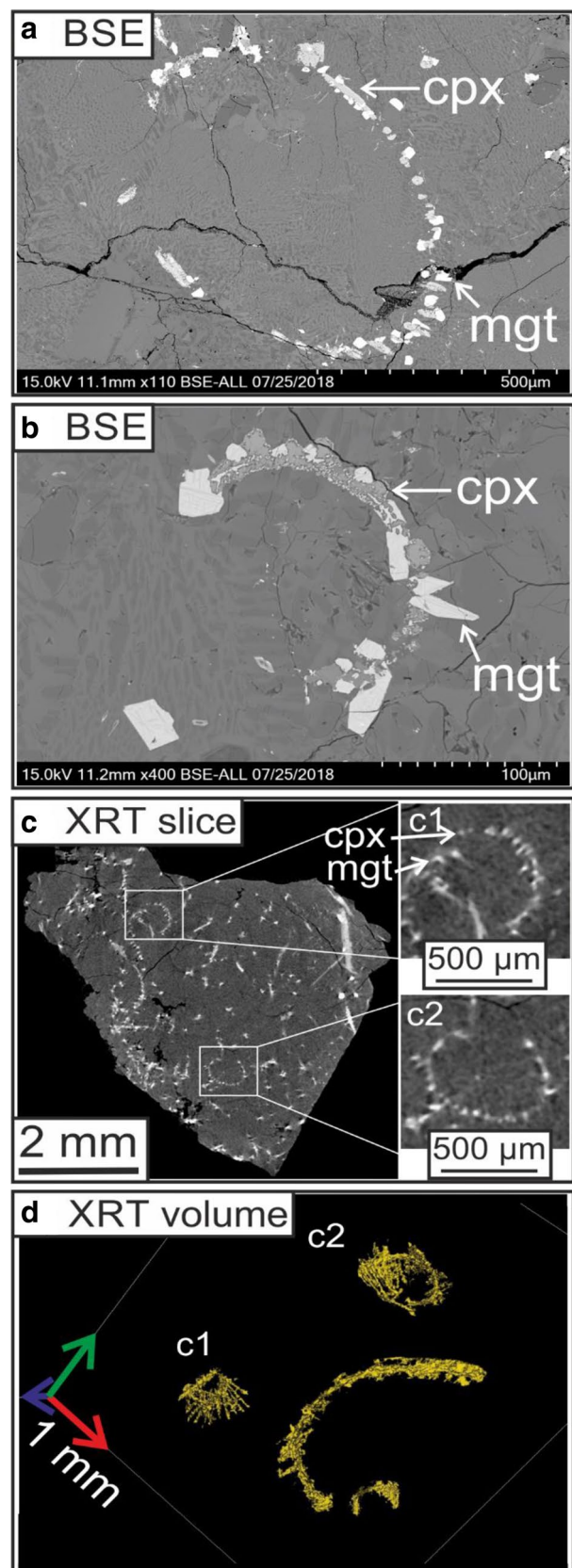
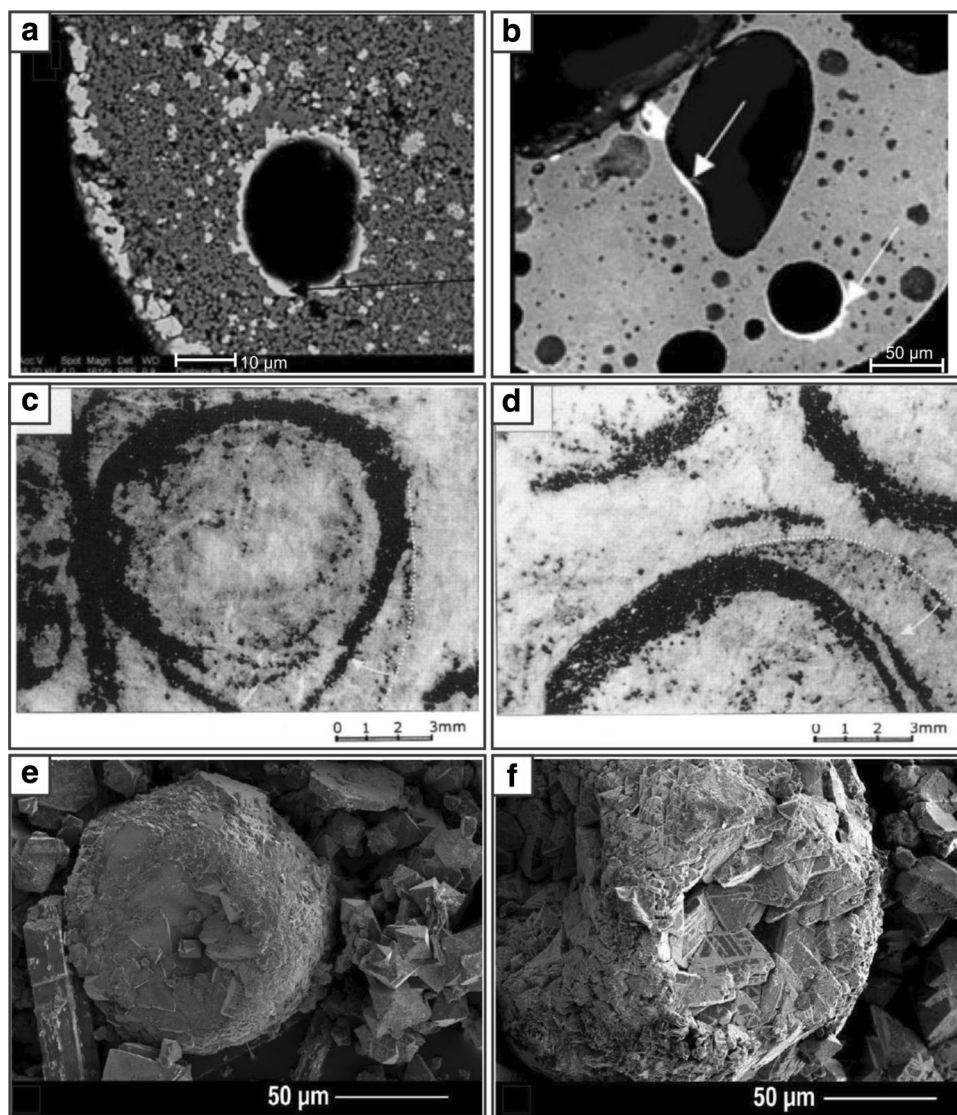


Fig. 8 A compilation of analogous structures found in literature. **a, b** Interior of a micrometeorite (Taylor et al. 2011), SEM images. The bubble in the center of image A is fully covered by a Fe–Ni oxide shell. The shell has a smooth interior and rugose outer surface. There are Fe–Ni oxides lining the micrometeorite border and within the melt. The two bubbles marked with arrows in image B have partial oxide shells. The smaller of the two has a smooth inner and rugose outer shell surface. **c, d** Orbicular chromite in a dunite matrix (Zhou et al. 2001), microscope images. The chromite in image C is highly similar to Fig. 2b. The outermost thin chromite shells in both images do not follow the concavity of the inner ones, which the authors interpreted as detachment. **e, f** Magnetite spherules from El Laco (Nyström et al. 2016), SEM images. The spherules have a hollow center and a densely packed shell of magnetite crystals (**a** and **b** from Taylor et al. 2011; **c** and **d** from; Zhou et al. 2001; **e** and **f** from; Nyström et al. 2016)



inner and rugose outer surface like the experimentally produced oxide shells (Fig. 8a, b), indicating growth from the melt rather than from vapor within the bubble. Crystallization from the melt is also supported by their occurrence in the melt away from the vesicles (see figures in Toppani et al. 2001; and Figs. 4b, 8b in; Taylor et al. 2011). These textures have an almost identical appearance to our oxide shells and we propose that they may have formed in the same way, by gas loss.

Orbicular chromite

Orbicular chromites (Fig. 8 c, d) consist of a shell of chromite crystals enveloping a roundish dunite (e.g., Greenbaum 1977) or serpentinite core (e.g., Yamane et al. 1988), in a matrix that is compositionally and texturally the same as the core. Textural features in common with our experimental oxide shells are a smooth inner and rugose outer surface,

several partly detached shell layers (Figs. 8 and 9 in Greenbaum 1977), collapsed shells and shells tracing out ghost cores (Fig. 3i, ii in Zhou et al. 2001). In the formation of orbicular chromites, the nucleation of chromite crystals and their growth could be similar to our oxide shells, i.e., in situ crystallization on a bubble or melt droplet (see Greenbaum 1977; Zhou et al. 2001; Matveev and Ballhaus 2002; Ballhaus et al. 2015).

El Laco magnetite deposit

The processes resulting in the extreme magnetite enrichment in one lava flow from the El Laco volcanic complex (Chile) remain enigmatic (Knipping et al. 2015; Ovalle et al. 2018). We looked for similarities between our oxide shells and the magnetite in this flow but found no explicit evidence of features like ours in published figures or descriptions. Although magnetite spherules found in the friable ore are similar to

our observations (Figs. 1e, 8e, f), no bubbles were observed at the center of these spherules (Nyström et al. 2016). It has been demonstrated experimentally that crystalline spherulites of $\text{Li}_2\text{Si}_2\text{O}_5$ can form by in situ nucleation on bubbles in melts (Davis and Ihinger 1998). Considering our evidence for the low preservation potential of oxide shells, we propose that the magnetite spherules may have originated in a similar way to that seen in our experiments, due to the lava flow's contact with the atmosphere. The scenario of bubble–oxide overturn and bubble escape through an upward orientated aperture in the oxide shell (as proposed in Fig. 6e) could be the reason why no bubbles were found in the center of El Laco spherules.

Conclusions

Our experimental results show that bubble–oxide aggregates with complex structures have the potential to form in andesitic magmas. Textural evidence including oxide shell morphology (smooth inner and rugose outer surfaces, skeletal growths), uniform size and low Ti content suggest these features were formed by in situ crystallization of oxides on the melt side of the bubble–melt interface. These results provide a glimpse into the events that lead to preferential oxide–bubble spatial distribution within volcanic rocks, suggest a probable mechanism for oxide transport by bubbles that has so far only been theoretically proposed, and answer the question why the initial textures have such a low preservation potential. These features, revealing dynamic mechanisms, could not have been identified through arbitrarily oriented and randomly chosen two-dimensional sections alone, highlighting the importance of three-dimensional observations.

We observed evidence for several different dynamic processes in the experiments: (1) daughter bubble generation through an oxide shell aperture, (2) detachment of oxide shells from bubble walls, (3) multiple oxide shells around a single bubble, (4) disintegration of oxide shell after detachment from the bubble. The potential consequences of these processes are the slowing of bubble ascent, continuous production of oxides at different depths and bubble breakup. Our experimentally produced oxide shells are texturally similar to natural textures from a range of geological environments, including magnetite + clinopyroxene structures in Krafla granophyres, Fe–Ni oxide shells around bubbles in micrometeorites, orbicular chromites and El Laco spherules.

The process of in situ crystallization at the bubble–melt interface is an alternative to harvesting that can be applied to bubbles of any gas (e.g., H_2O , H_2S , CO_2 , ...) passing through a magma bearing different elements and providing a surface for either crystal nucleation and growth, or crystal or immiscible melt accumulation. We suggest the same

process is behind all the above-mentioned occurrences; a phase (solid, crystal, or liquid, melt droplet) is forming (via different processes, in our case melt oxidation) and/or accumulating on the surfaces of another liquid phase (bubble or melt droplet, via harvesting) and is transported by it. As we have shown in our comparison to natural materials, the same process can occur with different crystals and on different surfaces (bubble–melt or melt–melt) and in different melt compositions.

Acknowledgements This research used resources of the Advanced Photon Source, a US Department of Energy (DOE) Office of Science User Facility operated for the DOE Office of Science by Argonne National Laboratory under Contract No. DE-AC02-06CH11357. Synchrotron imaging was performed at GeoSoilEnviroCARS (University of Chicago, Sector 13), Advanced Photon Source (APS), Argonne National Laboratory. GeoSoilEnviroCARS is supported by the National Science Foundation—Earth Sciences (EAR-1128799) and Department of Energy—GeoSciences (DE-FG02-94ER14466). The authors wish to thank John Stix and Kim Berlo for the use of the Krafla samples, and Chris Ballhaus and three anonymous reviewers for their work, which greatly enhanced the manuscript.

Author contributions PP (PhD student and principal investigator), MDH (PhD director) and DRB (PhD co-director) developed the ideas central to the manuscript. LM (beamline scientist) provided access to software and helped with the 3D data treatment, GL (post-graduate scientist) helped with the 3D analyses in Pore3D, MKP (graduate student) helped with the SEM analysis, and SR (graduate student) helped with natural samples. All authors helped with the writing of the manuscript.

Funding This work was supported by NSERC (Canada) Discovery grants to M.D.H. (RGPIN 2012–25137) and D.R.B. (RGPIN-2015-06355). The Student Travel/Research Grant awarded to P.P. in 2014 by the Mineralogical Association of Canada was used to cover the travel costs to APS.

Compliance with ethical standards

Conflict of interest The authors declare that they have no conflict of interest.

References

- Applegarth LJ, Tuffen H, James MR, Pinkerton H, Cashman KV (2013) Direct observations of degassing-induced crystallization in basalts. *Geology* 41(2):243–246
- Bai L, Baker DR, Rivers M (2008) Experimental study of bubble growth in Stromboli basalt melts at 1 atm. *Earth Planet Sci Lett* 267(3–4):533–547
- Baker DR (2004) Piston-cylinder calibration at 400 to 500 MPa: a comparison of using water solubility in albite melt and NaCl melting. *Am Mineral* 89(10):1553–1556
- Baker D, Eggler D (1987) Composition of melts coexisting with plagioclase, augite and olivine or low-calcium pyroxene at pressures from one atmosphere to 8 kbar, anhydrous and 2 percent H_2O and applications to island arc petrogenesis. *Am Mineral* 72:12–28
- Baker DR, Brun F, O'Shaughnessy C, Mancini L, Fife JL, Rivers M (2012) A four-dimensional X-ray tomographic microscopy study of bubble growth in basaltic foam. *Nat Commun* 3:1135

- Ballhaus C, Fonseca RO, Münker C, Kirchenbaur M, Zirner A (2015) Spheroidal textures in igneous rocks—Textural consequences of H₂O saturation in basaltic melts. *Geochim Cosmochim Acta* 167:241–252
- Boudreau AE (1995) Crystal aging and the formation of fine-scale igneous layering. *Miner Petrol* 54(1–2):55–69
- Brun F, Mancini L, Kasae P, Favretto S, Dreossi D, Tromba G (2010) Pore3D: a software library for quantitative analysis of porous media. *Nucl Instrum Methods A* 615(3):326–332
- Candela PA (1991) Physics of aqueous phase evolution in plutonic environments. *Am Mineral* 76
- Dalpé C, Baker DR (2000) Experimental investigation of large-ion-lithophile-element-, high-field-strength-element-and rare-earth-element-partitioning between calcic amphibole and basaltic melt: the effects of pressure and oxygen fugacity. *Contrib Mineral Petrol* 140(2):233–250
- Davis MJ, Ihinger PD (1998) Heterogeneous crystal nucleation on bubbles in silicate melt. *Am Mineral* 83(9–10):1008–1015
- Driesner T (2007) The system H₂O–NaCl. Part II: correlations for molar volume, enthalpy, and isobaric heat capacity from 0 to 1000 °C, 1 to 5000 bar, and 0 to 1 XNaCl. *Geochim Cosmochim Acta* 71(20):4902–4919
- Druitt TH, Young SR, Baptie B, Bonadonna C, Calder ES, Clarke AB, Cole PD, Harford CL, Herd RA, Luckett R, Ryan G, Voight B (2002) Episodes of cyclic vulcanian explosive activity with fountain collapse at Soufrière Hills Volcano, Montserrat. *Mem Geol Soc Lond* 21:281–306
- Dziewonski AM, Anderson DL (1981) Preliminary reference Earth model. *Phys Earth Planet Int* 25:297–356
- Edmonds M (2015) RESEARCH FOCUS: flotation of magmatic minerals. *Geology* 43(7):655–656
- Edmonds M, Brett A, Herd RA, Humphreys MCS, Woods A (2015) Magnetite-bubble aggregates at mixing interfaces in andesite magma bodies. *Geol Soc Lond Spec Publ* 410(1):95–121
- Eggler DH (1987) Solubility of major and trace elements in mantle metasomatic fluids: experimental constraints. In: Menzies M, Hawkesworth C *Mantle metasomatism*, Academic Press, Cambridge
- Fenn PM (1977) The nucleation and growth of alkali feldspars from hydrous melts. *Can Mineral* 15:135–161
- Gardner JE, Denis M-H (2004) Heterogeneous bubble nucleation on Fe–Ti oxide crystals in high-silica rhyolitic melts. *Geochim Cosmochim Acta* 68:3587–3597
- Gardner JE, Ketcham RA (2011) Bubble nucleation in rhyolite and dacite melts: temperature dependence of surface tension. *Contrib Mineral Petrol* 162(5):929–943
- Gnyloskurenko SV, Byakova AV, Raychenko OI, Nakamura T (2003) Influence of wetting conditions on bubble formation at orifice in an inviscid liquid. Transformation of bubble shape and size. *Colloid Surf A* 218(1–3):73–87
- Gonnermann HM, Gardner JE (2013) Homogeneous bubble nucleation in rhyolitic melt: experiments and nonclassical theory. *Geochem Geophys Geosyst* 14:1–16
- Greenbaum D (1977) The chromitiferous rocks of the Troodos ophiolite complex, Cyprus. *Econ Geol* 72(7):1175–1194
- Gualda GA, Anderson AT (2007) Magnetite scavenging and the buoyancy of bubbles in magmas. Part 1: discovery of a pre-eruptive bubble in Bishop rhyolite. *Contrib Mineral Petrol* 153(6):733–742
- Gualda GA, Ghiorso MS (2007) Magnetite scavenging and the buoyancy of bubbles in magmas. Part 2: energetics of crystal-bubble attachment in magmas. *Contrib Mineral Petrol* 154(4):479–490
- Harris JW, Stöcker H (1998) Spherical Wedge. § 4.8.6 in *handbook of mathematics and computational science*. Springer, New York, p 108
- Heath T (1987) *The works of Archimedes*. Cambridge University Press, Cambridge
- Holloway JR (1987) Igneous fluids. *Rev Mineral Geochem* 17(1):211–233
- Hurwitz S, Navon O (1994) Bubble nucleation in rhyolitic melts: experiments at high pressure, temperature, and water content. *Earth Planet Sci Lett* 122(3–4):267–280
- Ichihara M, Ohkunitani H, Ida Y, Kameda M (2004) Dynamics of bubble oscillation and wave propagation in viscoelastic liquids. *J Volcanol Geotherm Res* 129(1–3):37–60
- Jakobsson S (2012) Oxygen fugacity control in piston-cylinder experiments. *Contrib Mineral Petrol* 164(3):397–406
- Jónasson K (1994) Rhyolite volcanism in the Krafla central volcano, north-east Iceland. *Bull Volcanol* 56:516–528
- Kirkpatrick RJ (1977) Nucleation and growth of plagioclase, Makaopuhi and Alae lava lakes, Kilauea Volcano, Hawaii. *Geol Soc Am Bull* 88(1):78–84
- Knipping JL, Bilenker LD, Simon AC, Reich M, Barra F, Deditius AP, Lundstrom C, Bindeman I, Munizaga R (2015) Giant Kiruna-type deposits form by efficient flotation of magmatic magnetite suspensions. *Geology* 43(7):591–594
- Kushnir AR, Martel C, Champallier R, Arbaret L (2017) In situ confirmation of permeability development in shearing bubble-bearing melts and implications for volcanic outgassing. *Earth Planet Sci Lett* 458:315–326
- Lange RA, Carmichael IS (1987) Densities of Na₂O–K₂O–CaO–MgO–FeO–Fe₂O₃–Al₂O₃–TiO₂–SiO₂ liquids: new measurements and derived partial molar properties. *Geochim Cosmochim Acta* 51(11):2931–2946
- Lange RA, Carmichael IS (1996) The Aurora volcanic field, California-Nevada: oxygen fugacity constraints on the development of andesitic magma. *Contrib Mineral Petrol* 125(2–3):167–185
- Le Gall N, Pichavant M (2016) Homogeneous bubble nucleation in H₂O- and H₂O–CO₂-bearing basaltic melts: results of high temperature decompression experiments. *J Volcanol Geotherm Res* 327:604–621
- Liu Y, Samaha NT, Baker DR (2007) Sulfur concentration at sulfide saturation (SCSS) in magmatic silicate melts. *Geochim Cosmochim Acta* 71(7):1783–1799
- Mangan M, Sisson T (2000) Delayed, disequilibrium degassing in rhyolite magma: decompression experiments and implications for explosive volcanism. *Earth Planet Sci Lett* 183(3–4):441–455
- Matveev S, Ballhaus C (2002) Role of water in the origin of podiform chromitite deposits. *Earth Planet Sci Lett* 203(1):235–243
- Menzies M, Hawkesworth C (1986) *Mantle metasomatism*. Department of Energy, USA (OSTI ID: 5870369)
- Murphy MD, Sparks RSJ, Barclay J, Carroll MR, Brewer TS (2000) Remobilization of andesite magma by intrusion of mafic magma at the Soufriere Hills Volcano, Montserrat, West Indies. *J Petrol* 41(1):21–42. <https://doi.org/10.1093/petrology/41.1.21>
- Myers ML, Wallace PJ, Wilson CJ (2019) Inferring magma ascent timescales and reconstructing conduit processes in explosive rhyolitic eruptions using diffusive losses of hydrogen from melt inclusions. *J Volcanol Geotherm Res* 369:95–112
- Mysen BO, Richet P (2005) *Silicate glasses and melts: properties and structure*. Elsevier, Amsterdam
- Nyström JO, Henríquez F, Naranjo JA, Nasuland HR (2016) Magnetite spherules in pyroclastic iron ore at El Laco, Chile. *Am Mineral* 101(3):587–595
- Ochs FA III, Lange RA (1997) The partial molar volume, thermal expansivity, and compressibility of H₂O in NaAlSi₃O₈ liquid: new measurements and an internally consistent model. *Contrib Mineral Petrol* 129(2–3):155–165
- Ochs FA III, Lange RA (1999) The density of hydrous magmatic liquids. *Science* 283(5406):1314–1317
- Ovalle JT, La Cruz NL, Reich M, Barra F, Simon AC, Konecke BA, Rodriguez-Mustafa MA, Deditius AP, Childress TM, Morata D

- (2018) Formation of massive iron deposits linked to explosive volcanic eruptions. *Sci Rep* 8(1):14855
- Papale P, Moretti R, Barbato D (2006) The compositional dependence of the saturation surface of H₂O + CO₂ fluids in silicate melts. *Chem Geol* 229(1–3):78–95
- Phan CM, Nguyen AV, Miller JD, Evans GM, Jameson GJ (2003) Investigations of bubble–particle interactions. *Int J Miner Process* 72(1–4):239–254
- Pitzer KS, Sterner SM (1995) Equations of state valid continuously from zero to extreme pressures with H₂O and CO₂ as examples. *Int J Thermophys* 16(2):511–518
- Pleše P, Higgins MD, Mancini L, Lanzafame G, Brun F, Fife JL, Casselman J, Baker DR (2018) Dynamic observations of vesiculation reveal the role of silicate crystals in bubble nucleation and growth in andesitic magmas. *Lithos* 296:532–546
- Polacci M, Arzilli F, La Spina G, Le Gall N, Cai B, Hartley ME, Di Genova D, Vo NT, Nonni S, Atwood RC, Llewellyn EW (2018) Crystallisation in basaltic magmas revealed via in situ 4D synchrotron X-ray microtomography. *Sci Rep* 8:1–13
- Preuss O, Marxer H, Ulmer S, Wolf J, Nowak M (2016) Degassing of hydrous trachytic Campi Flegrei and phonolitic Vesuvius melts: experimental limitations and chances to study homogeneous bubble nucleation. *Am Mineral* 101(4):859–875
- Rivers ML (2012) tomoRecon: high-speed tomography reconstruction on workstations using multi-threading. *Developments in X-Ray tomography VIII*. *Int Soc Opt Photon* 8506:8506U
- Rivers ML, Wang Y, Uchida T (2004) Microtomography at GeoSoilEnviroCARS. *Developments in X-Ray tomography IV*. *Proc. SPIE* 5535. <https://doi.org/10.1117/12.562556>
- Rivers ML, Citron DT, Wang Y (2010) Recent developments in computed tomography at GSECARS. *Developments in X-Ray tomography VII*. *Proc. SPIE* 7804:09. <https://doi.org/10.1117/12.861393>
- Rooyackers SM, Wilson CJN, Schipper CI, Barker SJ, Allan ASR (2018) Textural and micro-analytical insights into mafic–felsic interactions during the Oruanui eruption, Taupo. *Contrib Mineral Petrol* 173(5):35
- Sæmundsson K (1991) Geology of the Krafla system. In: Gardarsson A, Einarsson Á (eds) *Náttúra Mývatns. Hid Íslenska Náttúrufræðifélag*, Reykjavík, pp 25–95 (in Icelandic)
- Schindelin J, Arganda-Carreras I, Frise E, Kaynig V, Longair M, Pietzsch T, Preibisch S, Rueden C, Saalfeld S, Schmid B, Tinevez JY (2012) Fiji: an open-source platform for biological-image analysis. *Nat Methods* 9(7):676
- Shea T (2017) Bubble nucleation in magmas: a dominantly heterogeneous process? *J Volcanol Geotherm Res* 343:155–170
- Skyscan NV (2011) NRecon user manual
- Stewart DB, Walker GW, Wright TL, Fahey JJ (1966) Physical properties of calcic labradorite from Lake County, Oregon. *Am Mineral* 51(1–2):177–197
- Taylor S, Jones KW, Herzog GF, Hornig CE (2011) Tomography: a window on the role of sulfur in the structure of micrometeorites. *Meteorit Planet Sci* 46(10):1498–1509
- Toppani A, Libourel G, Engrand C, Maurette M (2001) Experimental simulation of atmospheric entry of micrometeorites. *Meteorit Planet Sci* 36(10):1377–1396
- Vollinger M (2017) The oxidation state of Hawaiian magmas. Masters Thesis, University of Massachusetts Amherst, 590. https://scholarworks.umass.edu/masters_theses_2/590
- Voltolini M, Haboub A, Dou S, Kwon TH, MacDowell AA, Parkinson DY, Ajo-Franklin J (2017) The emerging role of 4D synchrotron X-ray micro-tomography for climate and fossil energy studies: five experiments showing the present capabilities at beamline 8.3.2 at the advanced light source. *J Synchrotron Radiat* 24(6):1237–1249
- Yamane M, Bamba M, Bamba T (1988) The first finding of orbicular chromite ore in Japan. *Min Geol* 38(212):501–508
- Zhou MF, Malpas J, Robinson PT, Sun M, Li JW (2001) Crystallization of podiform chromitites from silicate magmas and the formation of nodular textures. *Resour Geol* 51(1):1–6

Publisher's Note Springer Nature remains neutral with regard to jurisdictional claims in published maps and institutional affiliations.